# Mammogram Enhancement Using Intuitionistic Fuzzy Sets

He Deng, Wankai Deng, Xianping Sun, Maili Liu, Chaohui Ye, and Xin Zhou*

***Abstract*—*Objective*: Conventional mammogram enhancement methods use transform-domain filtering, which possibly produce some artifacts or not well highlight all local details in images. This paper presents a new enhancement method based on intuitionistic fuzzy sets. *Methods*: The presented algorithm initially separates a mammogram via a global threshold and then fuzzifies the image utilizing the intuitionistic fuzzy membership function that adopts restricted equivalence functions. After that, the presented scheme hyperbolizes membership degrees of foreground and background areas, defuzzifies the fuzzy plane, and achieves a filtered image via normalization. Finally, an enhanced mammogram is obtained by fusing the original image with filtered one. These implementations can be processed in parallel. *Results*: This algorithm can improve the contrast and visual quality of regions of interest. *Conclusion*: Real data experiments demonstrate that our method has better performance regarding the improvement of contrast and visual quality of abnormalities in mammograms (such as masses and/or microcalcifications), compared with classical baseline methods. *Significance*: This algorithm has potential for understanding and determining abnormalities.**

***Index Terms*—Image enhancement, intuitionistic fuzzy sets (FSs), mammogram.**

## I. Introduction

ABOUT 12.3% of women will contract breast cancer in their lifetime in the United States [1], and that cancer is the chief cause of death in women between the ages of 35 and 55 years [2]. Currently, the National Cancer Institute estimates that the number of new cases of breast cancer was 124.6 per 100 000 people per year, and the number of deaths was 22.2 per 100 000 people per year [1]. At present, the early detection is vital for treating this epidemic [3]. Several imaging techniques are used for breast examination, for example, ultrasound, X-ray imaging, magnetic resonance imaging (MRI), computerized tomography (CT), and positron emission tomography (PET). Among them, mammography (X-ray pictures) is mostly applied to detect and diagnose breast cancer [4]–[6], including digital mammography and film mammography. Digital mammography owns several advantages such as the good image quality and detectability, and low X-ray dose for dense breast, postmenopausal, and/or older women [7].

Due to the limitations of X-ray hardware systems, screened mammograms are undoubtedly degraded by different types of noise or blurred owing to the properties of imaging devices and image transmission. This potentially presents a low resolution or poor contrast, making it difficult to distinguish and diagnose breast diseases [2], [8]. Some methods are used to improve the visual quality of mammary images [9]–[11]. One is to collect more images at the data acquisition stage, which increases the overall acquisition time, the amount of radiation that a patient is exposed to, hardware costs, and radiologist's caseload [2], [3]. The other way is to improve the image quality during the image postprocessing stage, in order to better the contrast of specific regions and/or objects in mammograms without influencing the acquisition process or burdening the hardware costs [2].

Several enhancement algorithms have been used to improve the quality of mammograms, such as methods based on filtering, histogram equalization (HE), wavelet decomposition, or fuzzy sets (FSs) theory. They can be roughly categorized into spatial- and transformation-domain methods. Detailed reviews can be found in [12]–[14].

*Spatial-domain methods*: These approaches are based on the direct manipulation of intensities in images. Statistical based subband filtering methods are effective to enhance masses and calcifications in mammary images by inhibiting noise [15], but these methods possibly cause edge smearing and detail loss [8]. Adaptive enhancement algorithms are desirable to improve the contrast while preserving edges and details of mammograms, such as methods based on the adaptive neighborhood [3], [16], adaptive density weighted contrast [9], or first derivative and local statistics [17]. Although HE methods hold the dominant position in the field of enhancement, they potentially result in excessive contrast enhancement or washed-out effect owing to the lack of control on the level of enhancement [8]. Thus, some

Manuscript received July 18, 2016; revised September 22, 2016 and October 25, 2016; accepted October 27, 2016. Date of publication November 2, 2016; date of current version July 15, 2017. This work was supported in part by the Natural Science Foundation of China under Grant 81227902 and Grant 61471355 and in part by the National Program for Support of Eminent Professionals (National Program for Support of Top-Notch Young Professionals). *Asterisk indicates corresponding author.*

H. Deng, X. Sun, M. Liu, and C. Ye are with the Key Laboratory of Magnetic Resonance in Biological Systems, State Key Laboratory of Magnetic Resonance and Atomic and Molecular Physics, National Center for Magnetic Resonance in Wuhan, Wuhan Institute of Physics and Mathematics, Chinese Academy of Sciences.

W. Deng is with the Department of Head and Neck and Neurosurgery, Hubei Cancer Hospital.

*X. Zhou is with the Key Laboratory of Magnetic Resonance in Biological Systems, State Key Laboratory of Magnetic Resonance and Atomic and Molecular Physics, National Center for Magnetic Resonance in Wuhan, Wuhan Institute of Physics and Mathematics, Chinese Academy of Sciences, Wuhan 430071, China (e-mail: xinzhou@wipm.ac.cn).

Digital Object Identifier 10.1109/TBME.2016.2624306

methods are explored to overcome those deficiencies, e.g., the adaptive HE (AHE) and contrast-limited AHE (CLAHE) [18].

Unsharp masking (UM) is good at enhancing fine details of mammograms but amplifies noise and overshoots steep details at the same time [19]. Then, some modified schemes such as the rational UM (RUM) [19] and nonlinear UM (NUM) [2] are developed to conquer those issues. Sivaramakrishna *et al*. had compared the performance of wavelet transformation, CLAHE, adaptive UM, and adaptive neighborhood contrast enhancement (ANCE) methods and drawn the conclusion that the ANCE method was preferred most often [20].

*Transformation-domain methods*: These methods are based on the multiscale representation or FSs theory which uses an input/output transformation that changes with the local feature of a mammogram. Multiscale representation-based methods first decompose a mammogram into a multiscale subband representation via the contourlet, discrete dyadic wavelet, or integrated wavelets [21]–[23]. Next, they modify the transform coefficients in each subband and reconstruct a result from the modified coefficients. Nevertheless, this wavelet representation way does not efficiently display both the contour and geometry of edges in images [2].

Since the ambiguity and uncertainty are inevitably produced during the acquisition or transmission of mammograms, a valid mode portraying such images should utilize human knowledge expressed heuristically. However, this cannot be represented by the classical mathematical modeling [24]. Consequently, fuzzy theory, for example, FSs, logical FSs, type-I FSs, type-II FSs, or intuitionistic FSs (IFSs), are utilized to ameliorate the contrast and visual quality of images because they are knowledge-based techniques. These fuzzy methods effectively process imperfect data derived from vagueness and ambiguity [25]–[33].

However, the classical transformation-domain methods may generate artifacts called "objectionable blocking effects" [34], or enhance mammograms globally, but do not well enhance all local details/regions [2]. Moreover, the gray-level range of an output image applying type-I FSs is almost unchanged, which suggests that this method is unsuitable to enhance the degraded images with less gray levels and low contrast values [35], [36]. Type-II FSs are difficult to use and understand [37]. Therefore, mammogram enhancement is still a challenge.

In order to design a mammogram enhancement method, it is inspiring to adopt IFSs theory because IFSs take into account more uncertainties in the form of membership function that are more conformable to the aspects of human decision-making, in comparison to conventional FSs [36]. IFSs have attracted much attention in image processing field in recent years [38]–[43]. Among these methods, theoretical properties of IFSs model are studied from mathematical perspectives. As a result, the IFSs model is beneficial to guide the design of novel enhancement method. Notice that the nonlinear filtering is well known for its ability to suppress noise while preserving edges and fine details. With the earlier considerations in mind, a novel mammogram enhancement method inspired by the IFSs model and nonlinear filtering is designed in this paper.

Our method has two advantages. The first is that membership functions based on the restricted equivalence functions (REFs) are constructed. The constructed functions are appropriate for distinguishing different parts of an input mammogram. This is advantageous to discriminate specific regions of interest (ROIs). The second advantage is that a simple nonlinear mammogram enhancement algorithm is designed, which involves only three parameters. In this case, the designed algorithm is convenient to manipulate in applications. Experimental results verify that the designed method is an efficient and simple way to improve the contrast and visual quality of abnormalities, e.g., masses and/or microcalcifications in the mammogram. This suggests that the designed method has potential for understanding abnormal regions of mammary gland images.

The rest of this paper is organized as follows: In Section II, we review related work. In Section III, we present the designed mammogram enhancement algorithm in details. In Section IV, we give experimental results and discussions. And conclusions and perspectives are given in Section V.

## II. Related Work

This section briefly discusses theories of FSs and IFSs, and the framework of fuzzy image enhancement [36], [38]. These construct the basis of the novel enhancement scheme.

### A. Fuzzy Sets

Suppose that $U$ is a space of points set, an FS $A = \{(u, \mu(u), \nu(u)) | u \in U\}$ is represented by a membership function $\mu(u)$, where $u$ denotes a generic element of $U$. In this way, $\mu(u)$ is the membership degree, while $\nu(u)$ is the non-membership degree. The $\mu(u)$ associates a real number in an interval [0,1] with each point in $U$. When $A$ is a classical crisp set, its membership value takes on only two values 1 and 0, with $\mu(u) = 1$ or 0 according as $u$ does or does not belong to $A$.

An image is defined as an array of fuzzy singletons denoting membership value of each point. The definition of membership value depends on specific needs in specific applications. For example, the degree of brightness at pixel point $u$ in [35] is

$$\mu(u) = [1 + (u_{\max} - u)/\beta]^{-\alpha} \tag{1}$$

where $u_{\max}$ is the maximum gray value of the image and $\alpha$ and $\beta$ are the exponential and denominational fuzzifiers that regulate the amount of grayness ambiguity in the membership plane.

### B. Intuitionistic FSs

Besides the vagueness, IFSs offer a solid and mathematical setting to deal with the hesitancy derived from imperfect and/or imprecise information [38], [44]. IFSs reflect better the aspects of human behavior compared with the conventional FSs. For a finite set $U$, its IFS is

$$\begin{aligned} A = & \{(u, \mu(u), \nu(u), \omega(u)) | u \in U\} \\ \text{s.t.} & \begin{cases} \nu(u) = (1 - \mu(u))/(1 + \lambda \cdot \mu(u)) \\ \mu(u) + \nu(u) + \omega(u) = 1 \end{cases} \end{aligned} \tag{2}$$

where $\lambda$ is a constant in an interval [0,1] and the functions $\mu(u)$, $\nu(u)$, and $\omega(u)$ denote the membership degree, nonmembership

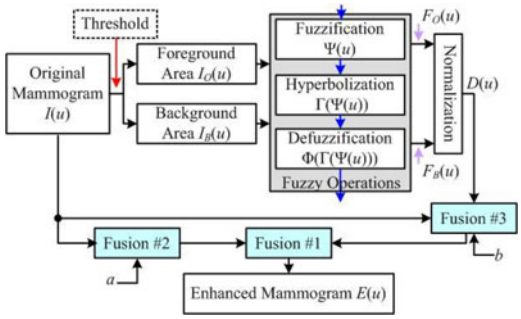


Fig. 1. Block diagram of the MIFS scheme, where *a* and *b* are the scaling factors.

degree, and hesitation degree. $\mu(u)$ can be constructed using REFs [45], logarithmic functions, exponential functions, *S* and *Z* functions, or others [42].

### C. Framework of Fuzzy Enhancement

There are three phases involved into the mostly fuzzy image processing approaches [36]:

1) Fuzzification $\Psi$, viz., the input data $U$ (histograms, gray levels, features, etc.) is converted into a membership plane.
2) Operation $\Gamma$, viz., some valid operator is applied in the membership plane for special applications, e.g., the enhancement and thresholding.
3) Defuzzification $\Phi$, viz., if necessary, the adjusted membership plane will be inversely converted into the characteristic plane, such as histograms, gray levels, features. Therefore, the output $X$ of the fuzzy system for an input $U$ is given by the following processing chain:

$$X = \Phi\left(\Gamma\left(\Psi\left(U\right)\right)\right) \tag{3}$$

The major difference to other methodologies in the image processing is that the input data $U$ is handled in the membership plane where one makes use of the diversity of FSs, IFSs, fuzzy logical, or fuzzy measure theories to modify and/or aggregate membership values, or classify data [36]. The new membership values are retransformed into the pixel plane to generate new characteristics, such as histograms, gray levels.

## III. MIFS

Integrating the fuzzy filtering (based on IFSs) with nonlinear fusion operators, we present a new fuzzy enhancement scheme, called as mammogram enhancement using intuitionistic fuzzy sets (MIFS), for mammogram enhancement in this section. This MIFS scheme is good at highlighting fine details, such as masses and/or microcalcifications in mammograms.

### A. MIFS Scheme

Since a foreground/background area has correlations in both spatial and frequency domain, it is necessary to divide an image into foreground and background areas for image enhancement. The block diagram of the MIFS scheme is shown in Fig. 1. An original mammogram $I(u)$ is separated into the foreground area $I_O(u)$ and background area $I_B(u)$ via a threshold. After that, the filtered areas [viz., $F_O(u)$ and $F_B(u)$] are achieved through fuzzy operations. Via normalization, the filtered mammogram $D(u)$ is combined with the original image by using the fusions #1, #2 and #3 to acquire an enhanced mammogram $E(u)$.

Steps for mammogram enhancement using an intuitionistic fuzzy algorithm are as follows.

*Step* 1: Separate a mammogram into the foreground area and background area.
*Step* 2: Construct intuitionistic fuzzification generators of the foreground and background areas, and then convert the pixel plane into a membership plane.
*Step* 3: Hyperbolize respective membership degrees of the foreground and background areas.
*Step* 4: Retransform the membership plane into a pixel plane, so achieve a filtered result through normalization.
*Step* 5: Obtain an enhanced result by combining the filtered result with the original image.

Forthcoming sections depict each step of the scheme briefly.

### B. Step 1: Selection of Threshold

Global thresholding methods are easy to implement and also computationally less involved [46], such as the Otsu, minimum error, and Parzen window estimate methods [47]. But each way has pros and cons. In this section, we adopt an iterative strategy to automatically divide a mammogram into the foreground and background areas. The selection of foreground or background does not require an input, for example, the indication of ROIs, the location of the breast, or the image feature from a user.

For an input mammogram, the following iterative strategy is used to find a global threshold, where $\lambda$ is a predefined constant.

1) Initialize the global threshold $T$, $T = 0.5 \cdot (I_{\max} + I_{\min})$, where $I_{\max}$ and $I_{\min}$ denote the maximum and minimum gray values of the mammogram.
2) Segment the mammogram using $T$. This engenders two groups of pixels: $I_1$ composing of all pixels with gray values $\geq T$, and $I_2$ consisting of pixels with values $<T$.
3) Calculate the average gray values $m_1$ and $m_2$ for the pixels in $I_1$ and $I_2$, respectively.
4) Compute a new threshold value: $\mathcal{T} = 0.5 \cdot (m_1 + m_2)$.
5) If $|T - \mathcal{T}| > \lambda$, let $T = \mathcal{T}$ and repeat Steps 2) through 4). Or else, achieve a final segmentation threshold $\mathcal{T}$.

### C. Step 2: Fuzzification

We use REFs to construct membership function of IFSs. If functions $\theta_1$ and $\theta_2$ are two automorphisms in a unit interval, an REF can be defined as

$$\begin{aligned} &\text{REF} : [0,1] \times [0,1] \rightarrow [0,1] \\ &\text{REF}\left(x, y\right) = \theta_1^{-1}\left(1 - \left|\theta_2\left(x\right) - \theta_2\left(y\right)\right|\right), \\ &\text{with } c\left(x\right) = \theta_2^{-1}\left(1 - \theta_2\left(x\right)\right) \end{aligned} \tag{4}$$

where $c(x)$ is a strong negation.

Let us consider $\theta_2(x) = x^2$, $0 \leq x \leq 1$. Hence, an REF is defined as $\text{REF}(x, y) = \theta_1^{-1}(1 - |x^2 - y^2|)$. Subsequently, let $\theta_1(x) = \log((e-1)x + 1)$. Through inverse function, we get $\theta_1^{-1}(x) = 0.582 \cdot (e^x - 1)$, where $e = \exp(1)$ and $1/(e -$

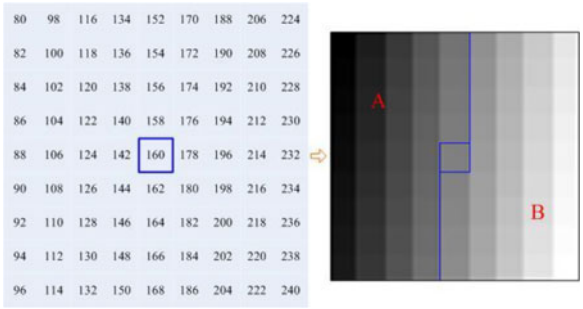


Fig. 2. Local gray area with size of 9 × 9 (left) and the corresponding gray map (right). The map is divided into the part *A* and part *B* according to the curve in the right column.

1) $\approx 0.582$. Therefore, the REF becomes

$$\mathrm{REF}\,(x,y) = 0.582 \cdot \exp\left(1 - |x+y| \cdot |x-y|\right) - 0.582. \tag{5}$$

It is easy to prove that the aforementioned function satisfies conditions of REFs. Different to (5), a Chaira's REF used in [38] was $\mathrm{cREF}(x,y) = 0.582 \cdot \exp(1-|x-y|) - 0.582$. Fig. 2 shows a local area of size 9 × 9 with 81 gray levels and the corresponding gray map. The average gray of this area is 160 (viz., the rectangular box). We divide the area into part *A* and *B* according to the average gray, where the line is the separatrix. If *x* denotes the gray value at point of part *A* or part *B* and *y* represents the average gray value of that part, the intuitionistic fuzzy divergence [38] between part *A* and part *B* is zero based on Chaira's REF (via normalization). In this way, part *A* so resembles part *B* in the membership plane, which is different from the original gray difference. This implies that Chaira's REF potentially results in misclassification in segmentation or classification. However, according to the proposed REF, the divergence between parts *A* and *B* is 0.3231 rather than 0 (the parameter in the intuitionistic fuzzy divergence is chosen as 0.85). This indicates that the REF based on (5) is appropriate to discriminate part *A* and part *B*.

After that, we utilize the gray value $x_u$ at point *u* in an image block (viz., the foreground or background area) to replace the variable *x*, and the average gray value of the block (viz., $m_O$ /$m_B$) to substitute the variable *y* in (5). Then, the fuzzification for the foreground area can be expressed as

$$\mu_O\,(u) = 0.582 \cdot \exp\left(1 - |x_u + m_O| \cdot |x_u - m_O|\right) - 0.582. \tag{6}$$

And the fuzzification for the background area is

$$\mu_B\,(u) = 0.582 \cdot \exp\left(1 - |x_u + m_B| \cdot |x_u - m_B|\right) - 0.582 \tag{7}$$

where $\mu_O(u)$ and $\mu_B(u)$ denote the membership functions of the foreground and background areas. The fuzzification function is considered as the belongingness of a pixel to the image block. When traversing the entire image, the pixel plane is converted into the membership plane according to (6) and (7).

### D. Step 3: Hyperbolization

After the fuzzification, a proper hyperbolization operation is necessary to enlarge the belongingness of the points whose gray levels are close to the average gray value of an image block and lessen the belongingness of those points whose gray levels are far from that average.

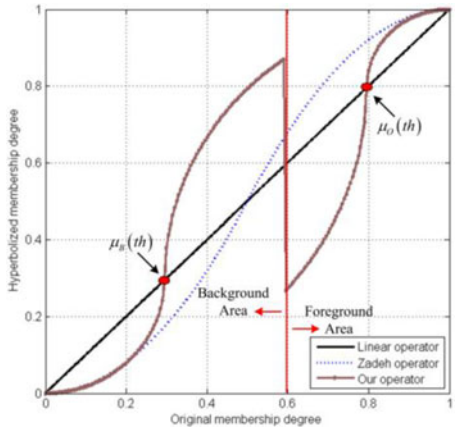


Fig. 3. Relationship between the original and hyperbolized membership degrees based on the linear, Zadeh, and proposed hyperbolization operators.

For membership degrees of a foreground area, we utilize the following hyperbolization:

$$\mu'_O\,(u) = \begin{cases} \mu_O\,(\mathrm{th}) - \sqrt{\mu_O^2\,(\mathrm{th}) - \mu_O^2\,(u)} \\ \text{if } (\mu_O)_{\min} \le \mu_O\,(u) \le \mu_O\,(\mathrm{th}) \\ \mu_O\,(\mathrm{th}) + \sqrt{(1-\mu_O\,(\mathrm{th}))^2 - (1-\mu_O\,(u))^2} \\ \text{if } \mu_O\,(\mathrm{th}) < \mu_O\,(u) \le (\mu_O)_{\max} \end{cases}$$
$$\text{where } \mu_O\,(\mathrm{th}) = 0.582 \cdot \exp\left(1 - |\mathrm{th} + m_O| \cdot |\mathrm{th} - m_O|\right) - 0.582. \tag{8}$$

And the hyperbolization for a background area is

$$\mu'_B\,(u) = \begin{cases} \mu_B\,(\mathrm{th}) - \sqrt{\mu_B^2\,(\mathrm{th}) - \mu_B^2\,(u)} \\ \text{if } (\mu_B)_{\min} \le \mu_B\,(u) \le \mu_B\,(\mathrm{th}) \\ \mu_B\,(\mathrm{th}) + \sqrt{(1-\mu_B\,(\mathrm{th}))^2 - (1-\mu_B\,(u))^2} \\ \text{if } \mu_B\,(\mathrm{th}) < \mu_B\,(u) \le (\mu_B)_{\max} \end{cases}$$
$$\text{where } \mu_B\,(\mathrm{th}) = 0.582 \cdot \exp\left(1 - |\mathrm{th} + m_B| \cdot |\mathrm{th} - m_B|\right) - 0.582 \tag{9}$$

where $\mu'_O$ and $\mu'_B$ are the hyperbolized membership degrees; th is the threshold according to the iterative strategy as mentioned earlier; $(\mu_O)_{\min}$ and $(\mu_O)_{\max}$, respectively, denote the minimum and maximum membership degrees of the foreground area; $(\mu_B)_{\min}$ and $(\mu_B)_{\max}$, respectively, denote the minimum and maximum membership degrees of the background area; and $m_O$ and $m_B$ denote the average gray values of the foreground and background areas, respectively.

As in Fig. 3, the theoretical relationship between the original and hyperbolized membership degrees is displayed, where the solid line, the dotted curve, and the solid curve denote the graphs of hyperbolized functions according to the linear, Zadeh [35] (the crossover point is set as 0.5), and the proposed hy-

perbolization operators. The vertical line is the division surface between the foreground and background areas. The $\mu_B(\text{th})$ in (9) is set to 0.2950, and the $\mu_O(\text{th})$ in (8) is viewed as 0.7950. The selection of $\mu_B(\text{th})$ and $\mu_O(\text{th})$ in this case is random. In applications, these parameters can be automatically determined according to (8) and (9) once given a mammogram (Since an image is given, the threshold is decided according to the earlier iterative strategy. After that, the foreground/background area is divided by using the threshold. Then, the average gray values of foreground/ background areas are defined. And finally, the $\mu_B(\text{th})$ and $\mu_O(\text{th})$ are achieved.) It can be found from Fig. 3 that the difference of two parts in the hyperbolized membership plane is augmented via the proposed hyperbolized operator. This is useful to improve the contrast of specific ROIs.

### E. Step 4: Defuzzification

Through Step 3, we gain hyperbolized membership degrees at each point in foreground/background area. If necessary, the hyperbolized membership plane is retransformed into a pixel plane through defuzzification operation.

Accordingly, the defuzzification for the foreground area is

$$F_O(u) = \begin{cases} \sqrt{m_O^2 + 1 - \log\left(1 + 1.718 \cdot \mu'_O(u)\right)} \\ \qquad \text{if } m_O \le x_u \le x_{\max} \\ \sqrt{m_O^2 - 1 + \log\left(1 + 1.718 \cdot \mu'_O(u)\right)} \\ \qquad \text{if th} \le x_u < m_O \end{cases}. \tag{10}$$

And the defuzzification for the background area is

$$F_B(u) = \begin{cases} \sqrt{m_B^2 + 1 - \log\left(1 + 1.718 \cdot \mu'_B(u)\right)} \\ \qquad \text{if } m_B \le x_u \le \text{th} \\ \sqrt{m_B^2 - 1 + \log\left(1 + 1.718 \cdot \mu'_B(u)\right)} \\ \qquad \text{if } x_{\min} \le x_u < m_B \end{cases} \tag{11}$$

where $F_O$ and $F_B$ denote the new gray value at the pixel point in foreground and background areas, and $x_{\min}$ and $x_{\max}$ denote the minimum and maximum gray values of the original image.

As a result, a normalized mammogram is achieved through

$$D(u) = \Delta(F_u) = (F_{\max} - F_u) / (F_{\max} - F_{\min}) \tag{12}$$

where $F_u$ is the value at point $u$ in the new pixel plane and $F_{\max}$ and $F_{\min}$ are, respectively, the maximum and minimum values of the new pixel plane, respectively.

### F. Step 5: Fusion

For different applications, the fusions #1, #2, and #3 shown in Fig. 1 could be chosen as the arithmetic or logic operations, or parameterized logarithmic image processing (PLIP) [48]. This property helps the MIFS fulfill more general and complicated demands for different applications. Since arithmetic operations show better performance than PLIP [2], we adopt the arithmetic addition and multiplication for the MIFS in this paper. Then the enhanced mammogram is

$$\begin{aligned} &E(u) = a \cdot I(u) + b \cdot (D(u) \otimes I(u)) \\ &\text{where } D(u) = \Delta(\Phi(\Gamma(\Psi(I(u))))) \end{aligned} \tag{13}$$

TABLE I
MOS RATING SCALE

| Rating | Image Quality | Distortion |
|---|---|---|
| 5 | Excellent | Imperceptible |
| 4 | Good | Just perceptible, not annoying |
| 3 | Fair | Perceptible, slightly annoying |
| 2 | Poor | Annoying, but not objectionable |
| 1 | Bad | Very annoying, objectionable |

where $a$ and $b$ are the scaling factors; $I(u)$ denotes the original mammogram; functions $\Psi$, $\Gamma$, $\Phi$, and $\Delta$ denote the fuzzification, hyperbolization, defuzzification, and normalization operations implemented orderly on $I(u)$; and $\otimes$ is the dot-product operation.

## IV. EXPERIMENTAL RESULTS

In this section, we first introduce the evaluation metrics, baseline methods, and data for comparison. After that, we utilize abundant mammograms selected from some cancer hospitals to demonstrate the effectiveness of the proposed method.

### A. Metrics, Baseline Methods, and Data

The mean opinion score (MOS) is a general measure used in the subjective evaluation of image enhancement [2], depending on the visual acuity of observers. The MOS is recommended by the IEEE Subcommittee on Subjective Methods and International Telecommunications Union. The MOS uses five-scale rating of image quality, as shown in Table I. The observers can describe their impression of the image quality only in five discrete steps according to the defined scale.

Besides MOSs, some objective measures have been explored to measure the enhancement performance of different methods, such as the Weber-law-based contrast measures, Michelson law measures of enhancement, and logarithmic Michelson contrast measures. However, these measures are sensitive to noise and steep edges in images [2]. As a result, we utilize the contrast ($C$) [21], contrast improvement (CI), region contrast (RC) [10], and RC improvement (RCI) as metrics in comparison of different enhancement methods. The contrast is independent of the actual range of gray levels in image, and the RC is insensitive to the noise and jitter [10]. For an image $I$, the definitions of $C$, CI, RC, and RCI are given as

$$\begin{aligned} &C = (C_o - C_b) / (C_o + C_b) \\ &\text{and } CI = C_{\text{Enhanced}} / C_{\text{Original}} \\ &RC = \frac{1}{m \times n} \sum_{(i,j) \in \Omega} |c(i,j)| \cdot \log(1 + |c(i,j)|) \\ &\text{and } \text{RCI} = \text{RC}_{\text{Enhanced}} / \text{RC}_{\text{Original}} \\ &\text{where } c(i,j) = 4I(i,j) - \{I(i-1,j) \\ &+ I(i,j-1) + I(i+1,j) + I(i,j+1)\} \end{aligned} \tag{14}$$

where $C_o$ and $C_b$ denote the average gray values of object and background areas in the image, $C_{\text{Enhanced}}$ and $C_{\text{Original}}$

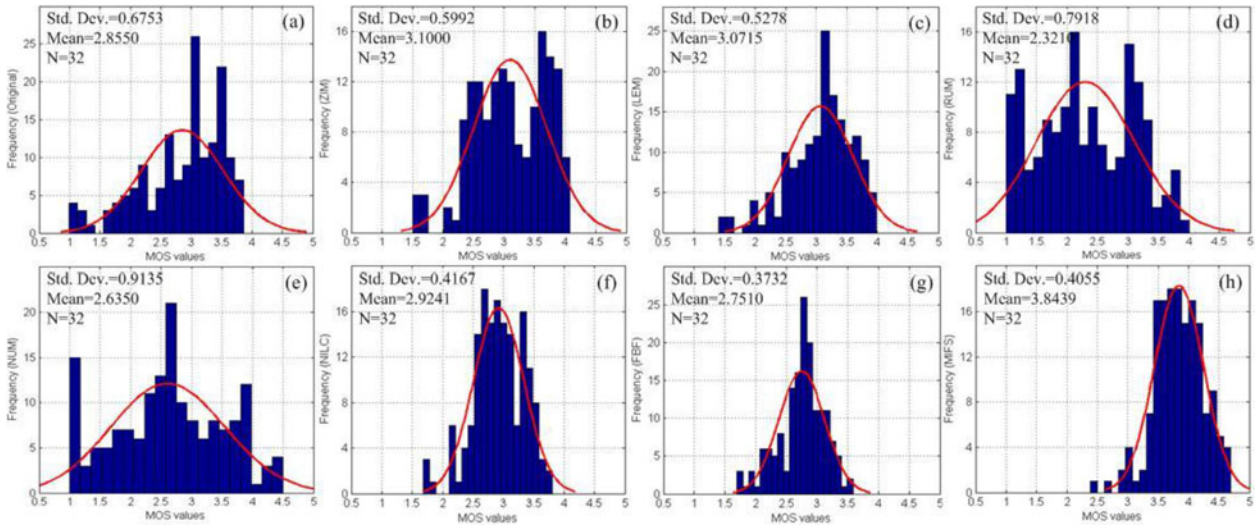


Fig. 4. MOS histograms of original and enhanced mammograms through different algorithms. (a) MOS histogram of original images. (b)−(h) MOS histograms of enhanced images obtained by using the ZIM, LEM, RUM, NUM, NILC, FBF, and MIFS algorithms. Where Mean and Std. Dev. denote the mean and standard deviation of MOS values, *N* denotes the number of images, and the red curves denote the fitted Rician curves, respectively.

denote the contrast values of enhanced and original images, $I(i, j)$ denotes the gray value at point $(i, j)$, $\Omega$ denotes a region of the image (the size of $\Omega$ is $m \times n$), and $RC_{\text{Enhanced}}$ and $RC_{\text{Original}}$ denote the RC values of enhanced and original ROIs, respectively. For each subjective/objective measure, a higher value denotes the better enhancement performance.

Since the MIFS method involves the fuzzy filtering process and fusion process, we use two fuzzy enhancement techniques as baseline methods, including Zadeh's intensification method (ZIM) [35] and lambda-enhancement method (LEM) [36]. The RUM [19] and NUM [2] fuse the filtered portion of a mammogram with the original one, which is similar to the MIFS. Hence, the RUM and NUM are also used as baseline algorithms for comparison. Moreover, the proposed method is compared with some recently proposed enhancement ways, namely, the nonuniformly illuminated and low-contrast enhancement algorithm (NILC) [49] and the fast bilateral filter algorithm (FBF) [50].

We used 32 mammograms randomly selected from Tianjin Cancer Hospital and Hubei Cancer Hospital, China, to validate the enhancement performance of the proposed MIFS algorithm. Some experimental results are shown in Tables III to VIII and Figs. 4−11. According to the breast disease types, the test mammograms were classified into seven groups, denoted as Groups 1 to 7 (16 patients were involved in this study). Details regarding the number of patients, patient age (years), number of images, and breast disease pathology for each group are listed in Table II. Moreover, the window/leveling was fixed on all original and filtered images. The fixed window/level matched to the original mammograms.

### B. Enhancement Measures

A set of 32 test mammograms is randomly selected from Tianjin Cancer Hospital and Hubei Cancer Hospital. All test images are processed using the ZIM, LEM, RUM, NUM, NILC, FBF, and MIFS methods. Hence, including the original and processed mammograms, there are 256 test images in total $(32 \times 8 = 256)$ for both subjective and objective comparisons.

In the subjective evaluation test, five experts, including three radiologists and two surgeons majoring in the mammary gland diseases visually evaluated all original and processed images. Each expert has at least ten years of experience in the related field. All the observers were unaware of which method was used in processed images, and all test images were in a random order. The observers assessed and gave a score for every test image. This resulted in eight MOS matrices with size of $32 \times 5$.

The MOS histogram of original mammograms is displayed in Fig. 4(a), where the vertical axis denotes the frequency and the horizontal axis denotes the MOS levels. The number of bars in the histogram is set to 20. The number of images, mean and standard deviation of MOS scores, and fitted Rician curve are also displayed in Fig. 4(a). The mean MOS score of original images is 2.8550, which suggests that the original quality is fair and the distortion is perceptible and slightly annoying. After the ZIM, LEM, RUM, NUM, NILC, FBF, and MIFS methods, the corresponding MOS histograms of processed mammograms are shown in Fig. 4(b)–(h), respectively. The meaning of graphs is the same as that shown in Fig. 4(a), viz., the number of bars in histograms is always set to 20, and the data is fitted through the Rician distribution. The mean MOS score listed in Fig. 4(d) is 2.3210, which implies that the visual quality of results obtained by using the RUM method is somewhat poor and the distortion is annoying. The visual quality of processed images obtained by using the ZIM and LEM is fair, and the distortion is slightly annoying. However, the mean MOS score shown in Fig. 4(h) is 3.8439. This indicates that the visual quality of results obtained by using the MIFS algorithm is some good and the distortion is slightly perceptible and not annoying.

Table III displays the average subjective evaluation scores of each observer for original and processed images categorized

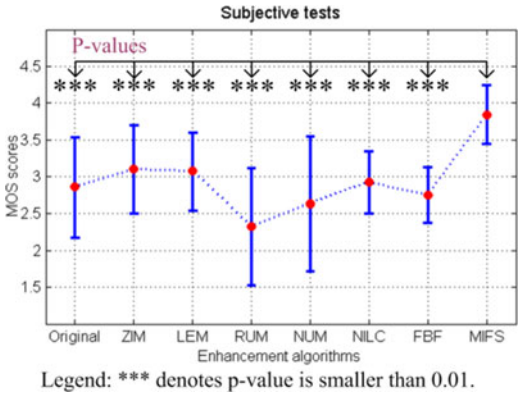


Fig. 5. Statistical analysis of subjective evaluation scores.

by the ZIM, LEM, RUM, NUM, NILC, FBF, and MIFS methods. Based on the scores, the MIFS method achieves the best overall visual quality with scores of 4.0753, 3.7185, 3.8046, 3.9095, and 3.7118, while the RUM method obtains the worst quality with scores of 2.9978, 1.6586, 2.3994, 1.9675, and 2.5819.

The subjective evaluation scores were tested for significant differences using a two-tailed Student's *t*-test. Fig. 5 displays the statistical analysis of MOS scores, where the vertical axis denotes MOS scores, and the horizontal axis denotes different enhancement methods. The *p*-values are statistical differences between the MOS scores of results obtained by using the MIFS and the MOS scores of the original images or results acquired by using the ZIM, LEM, RUM, NUM, NILC, and FBF methods. The error bars denote the mean $\pm$ standard deviation of MOS scores. From Fig. 5, we can find that all the *p*-values in multiple comparisons are smaller than 0.01. This indicates that the MIFS is statistically significantly different to the original as well as baseline methods in MOS comparison.

After that, we utilize four objective indexes (viz., *C*, CI, RC, and RCI) to measure the image quality of all 256 test mammograms. For the calculation of *C* and CI, some experts initially identified the true object (e.g., the mass and/or calcification), then the rectangular object area surrounding the true object were determined. Similar to the calculation of *C* and CI, some experts first chose the rectangular ROI, and then the RC and RCI were computed in this ROI.

For each group of mammograms, Table IV lists the contrast values of the original or processed images classified by the ZIM, LEM, RUM, NUM, NILC, FBF, and MIFS algorithms. The measure results listed in Table IV are average contrast values of each group. It can be seen that different enhancement methods produce diverse measure results for the original and processed images. Table IV indicates that the MIFS gives the best visual quality with scores of 0.4207, 0.5011, 0.6296, 0.6335, 0.5136, 0.6144, and 0.7571, and the ensemble average contrast value is 0.5814. However, the RUM obtains the worst visual quality with scores of 0.2466, 0.2952, 0.2957, 0.2970, 0.2443, 0.3089, and 0.3597, and the ensemble average value is 0.2925. Similar to Table IV, the measure results shown in Table V are average CI values of each group. It can be found from Tables IV and V that the MIFS is superior to the baseline methods with respect to the *C* and *CI*.

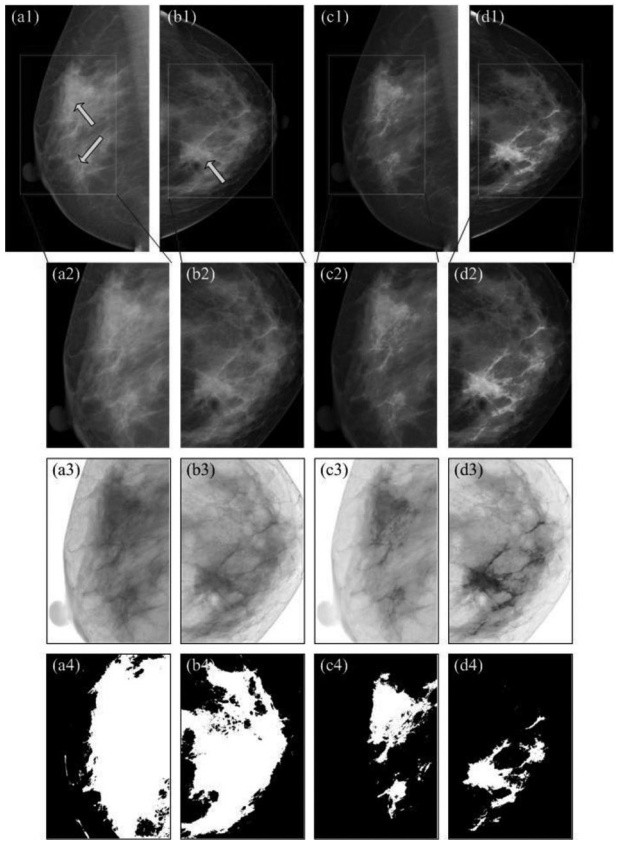


Fig. 6. Enhancement analysis. Top row, from left to right, are (a1) the original image of the left breast with IDC, (b1) original image of the right breast with IDC, and (c1) the enhanced results of the left and (d1) right breasts obtained by using the MIFS algorithm, where the arrows indicate the locations of abnormalities. Cropped regions delineated by the rectangles in the top row are shown in the second row (a2)–(d2), the negative grayscale regions are shown in the third row (a3)–(d3), and the thresholding of cropped regions are shown in the fourth row (a4)–(d4).

In addition, Table VI lists the average RC values of original and processed images obtained by using different enhancement algorithms for each group. The RCI values are listed in Table VII. For seven groups of mammograms, the MIFS scheme achieves the RC values with scores of 2.5803, 1.9624, 5.8578, 3.7921, 3.3986, 3.6373, and 3.1642, as well as the RCI values with scores of 1.7130, 1.6134, 2.3911, 1.9906, 1.8301, 2.3480, and 1.9935, respectively. The earlier objective measures (viz., *C*, CI, RC, and RCI) indicate MIFS-enhanced mammograms as the best. It is in accord with the conclusion derived from the MOS evaluation results.

### C. Enhancement Analysis

Many different methods can be used to analyze enhancement results, such as the negative view as well as the thresholding of designated ROIs. Fig. 6(a1) and (b1) shows two mammograms with infiltrating ductal carcinoma (IDC), where arrows indicate the location of IDC. The boundaries between the normal and abnormal tissues are much blurry. Through the MIFS method, the enhanced results are displayed in Fig. 6(c1) and (d1). It can be seen that the abnormal regions is clear and easily

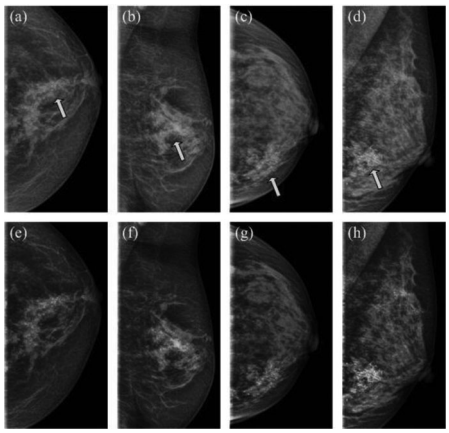


Fig. 7. Enhancement of IC mammograms. Upper row (from left to right) (a)–(d): original images, where the arrows indicate the locations of abnormalities. Lower row (e)–(h): the corresponding enhanced results obtained by using the MIFS algorithm.

discernible. The cropped regions delineated by the rectangles in Fig. 6(a1)−(d1) are shown in (a2)−(d2). The negative photographs and thresholding of specific ROIs are displayed in Fig. 6(a3)−(d3) and (a4)−(d4), respectively. It can be found that the lesions are more easily recognizable in enhanced results, when compared with original mammograms. The window/level set for ROIs in the enhanced and nonenhanced mammograms are the same.

A radiologist primarily concentrates on bright areas of a film when he or she diagnoses a mammogram [3]. If the gray level range of an abnormal region is enlarged, the details in ROIs will be highlighted. As shown in Fig. 6, the contrast/shape/details of the IDC regions is improved in the enhanced results. In this way, the improvement is valuable to a radiologist or nonradiologist reader for understanding those abnormalities. Fig. 6 verifies the MIFS scheme efficient performance for improving the contrast of specific regions and/or details in mammograms.

Four original mammograms with intraductal carcinoma (IC) are shown in Fig. 7(a)–(d), and the locations of abnormalities are marked by the arrows. We can see that there is obscure contrast/density difference between the lesions and surrounding normal tissues. However, after the MIFS algorithm, that difference is amplified, as shown in Fig. 7(e)–(h). Then, the abnormalities are easily delineated. This is helpful for surgeons and radiologists to discriminate and diagnose mammary gland diseases.

Furthermore, all nonenhanced and enhanced mammograms obtained by using the MIFS are assessed by several radiologists from Hubei Cancer Hospital. Compared with original images, they agree on the following:

1) Fig. 6 extracts and separates adipose tissues, normal gland, and suspicious lesion areas. In this case, it can not only decrease the interference of overlapping images but also better the diagnostic efficiency of high positive regions.

2) The enhanced results better the visualization of lesion features (such as the density, shape, and edge) and the structure of adjacent tissues, as shown in Figs. 6 and 7.

3) The distribution of masses and/or microcalcifications is clearer in the enhanced results, as shown from Figs. 7 to 11.

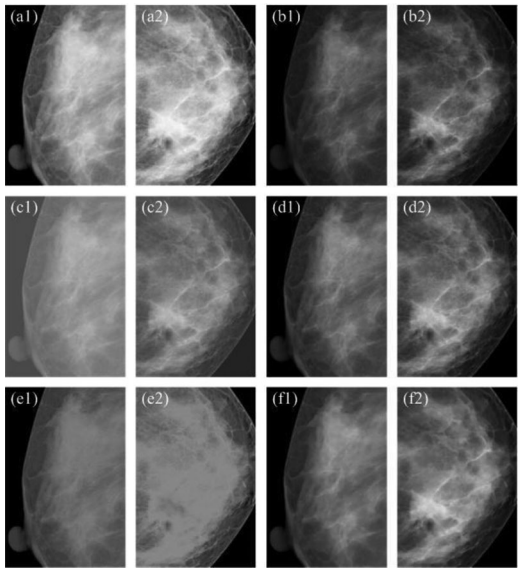


Fig. 8. Enhancement comparison. (a1) and (a2), (b1) and (b2), (c1) and (c2), (d1) and (d2), (e1) and (e2), and (f1) and (f2) enhanced results of Figs. 6(a1) and (b1), obtained by using the ZIM, LEM, RUM, NUM, NILC, and FBF methods, respectively.

This is helpful to accurately outline the range and location of lesions that tend to response the actual infiltration area of cancer focus.

4) The enhanced results can clearly reflect the lucent bubbles in the parenchyma and enlarge the density difference in the compact cancers. The trabecula and vessels around the lesions are sharper in enhanced results.

### D. Enhancement Comparison

For the images with IDC shown in Fig. 6(a1) and (b1), the filtered results obtained by using the ZIM, LEM, RUM, NUM, NILC, and FBF methods are displayed in Fig. 8(a1) and (a2), (b1) and (b2), (c1) and (c2), (d1) and (d2), (e1) and (e2), and (f1) and (f2), respectively. These filtered mammograms are cropped into images with small sizes for analysis according to the ROIs size. The baseline methods slightly improve the visual quality of the right breast image [viz., Fig. 6(b1)/(b2)] except the NILC. However, all the baseline algorithms have very limited visual improvement for the left breast mammogram [viz., Fig. 6(a1) or (a2)]. Especially, the NILC overenhances lesion regions of both the left and right mammary gland images, making the lesions more unidentifiable than the original ones. Besides, the RUM overenhances the background of the images. Comparing Fig. 6 with Fig. 8, it can be seen that the proposed method is superior to the baseline methods because the abnormal regions in Fig. 6(c2) and (d2) are clearer and more recognizable.

The enhanced results of IC mammograms obtained by using the six baseline methods are shown in Fig. 9(a1)−(a4), (b1)−(b4), (c1)−(c4), (d1)−(d4), (e1)−(e4), and (f1)−(f4). Comparing Fig. 7 with Fig. 9, the proposed method generates better visual quality and local contrast. Moreover, it can be seen that the fine details in Fig. 7 are distinctly improved, and the abnormal regions (for example masses and/or microcalcifica-

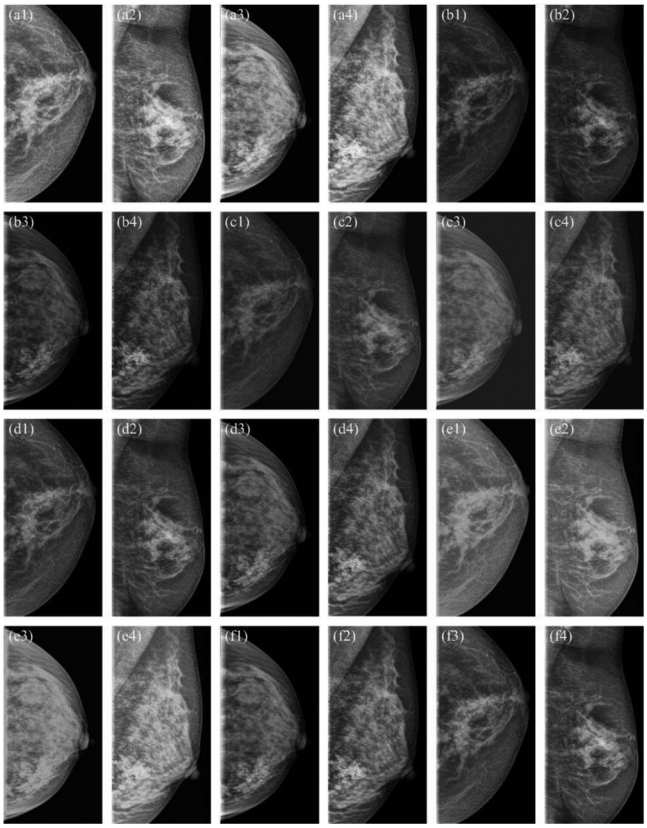


Fig. 9. Enhanced results of IC images obtained by using the baseline methods. (a1)–(a4), (b1)–(b4), (c1)–(c4), (d1)–(d4), (e1)–(e4), and (f1)–(f4) enhanced results obtained by using the ZIM, LEM, RUM, NUM, NILC, and FBF algorithms.

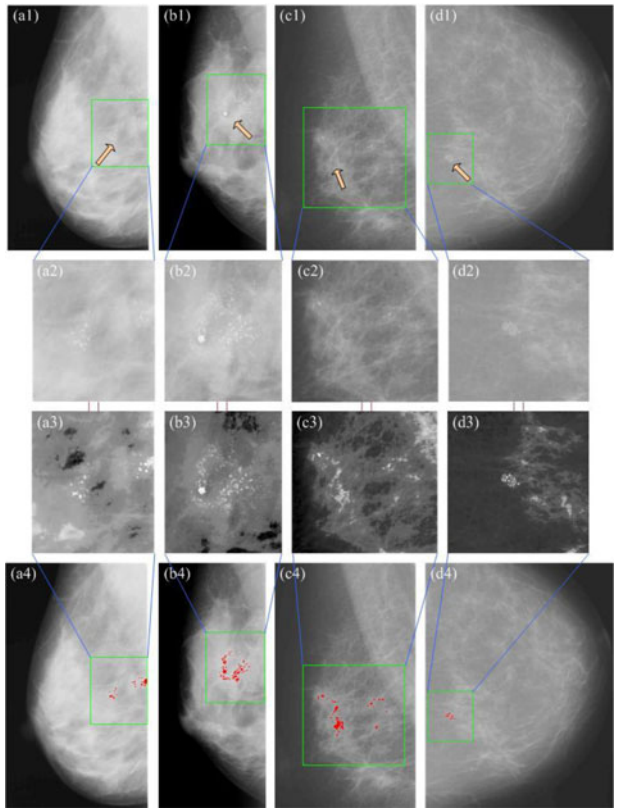


Fig. 10. Enhancement of ROIs. Top row (a1)–(d1): Original mammograms with masses and/or microcalcifications. Cropped ROIs delineated by the rectangles in the top row are shown in the second row (a2)–(d2), where the arrows indicate the location of abnormalities. The enhanced results of (a2)–(d2) obtained by using the MIFS algorithm are shown in the third row (a3)–(d3), and the original mammograms superimposed by the enhanced ROIs are shown in the fourth row (a4)–(d4).

tions) are more discriminable. In this way, the MIFS is helpful to discriminate abnormalities in mammograms.

The subjective and objective measure results (viz., MOS, $C$, CI, RC, and RCI) shown in Tables III to VII demonstrate this as well. Consequently, the quantitative and qualitative comparison demonstrates that the MIFS algorithm has better enhancement performance than the baseline methods. This is advantageous to discriminate and diagnose the abnormalities in mammograms, guide the operation, judge the prognosis, and conveniently plan the radiotherapy.

### *E. Regions of Interest*

When a radiologist views a digitized mammogram, he or she usually observes the architectural abnormalities and describes their locations, that is, selects an ROI. If an enhanced version of ROI presents alongside the original image, the radiologist can switch between the original mammogram and the automatically enhanced views for comparison. Accordingly, he or she can easily delineate any new details or features which are apparent to him or her, even identify some subtle findings in mammograms.

Four mammograms with masses and/or microcalcifications are displayed in Fig. 10(a1)–(d1), where the arrows point out the locations of the abnormalities. The green rectangles indicate the ROIs selected by a radiologist, as shown in Fig. 10(a2)–(d2). We can see that the contrast of abnormalities is faint. Nevertheless, through the MIFS method, the enhanced results are shown in Fig. 10(a3)–(d3). It can be found that both the visual quality and contrast of the enhanced ROIs are much better than that of the original ones. To synchronously show enhanced abnormalities as well as normal tissues, the enhanced ROIs are superimposed in the corresponding original mammograms, as shown in Fig. 10(a4)–(d4), where the red areas consisting of some pixels denote the detected masses and/or microcalcifications. These pixels are segmented via a global threshold in enhanced ROIs and the segmentation results are refined by postprocessing.

The detected masses and/or microcalcifications are assessed by a female surgeon majoring in the mammary gland diseases. She considers that the detected results are accurate reflections of abnormal regions (e.g., lesions) in mammograms. Moreover, these results are helpful to discern and diagnose breast diseases or cancers.

In general, the MIFS algorithm is able to effectively improve the contrast as well as visual quality of abnormalities in images. This suggests that the MIFS has potential for understanding the lesions and identifying subtle findings by enhancing fine details in mammograms, and then improving the disease detection.

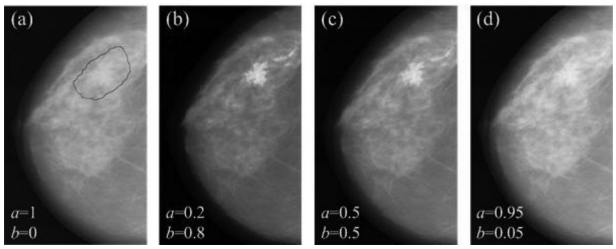


Fig. 11. Effects of scaling parameters in (13). From left to right: (a) original mammogram and (b)–(d) enhanced results under different scaling factors.

### F. Discussion

In this paper, a novel mammogram enhancement algorithm (MIFS) was presented to effectively highlight the fine details in mammograms. The MIFS scheme can derive different variants: 1) The user can adopt other thresholding methods to separate the foreground and background areas (e.g., the adaptive threshold or local threshold), in order to accommodate more complex and specific requirements in real applications. 2) The membership function can be derived from other types of intuitionistic fuzzy generators, such as $S$ and $Z$ functions, exponential functions, or logarithmic functions. 3) The fuzzy operation can be rooted in other fuzzy filtering algorithms, for example, type-II FSs, fuzzy HE, or fuzzy logical approaches. In addition, this operation can be designed as a combination of two or more various types of filters. 4) These are three coefficients involved in the MIFS (If given some reasonable assumptions in specific applications, those coefficients could be characterized by fewer variables), which can simplify the MIFE design. Generally, the MIFE scheme can be represented by two properties. One is that different types of intuitionistic fuzzy generators or fuzzy filters can be embedded into the MIFS scheme. The other property is that the segmentation threshold, scaling coefficients and fusion operators allow users to change the MIFS characteristics for the application-specific requirements or reasonable assumptions.

The selection and determination of some parameters used in analytical considerations should be rational. If a user makes a proper assumption owing to practical design requirements, the number of parameters will be reduced. For example, the sum of scaling parameters $a$ and $b$ in (13) was set to 1. An original mammogram with mass is shown in Fig. 11(a), where the black curve denotes the location of the mass. It can be found that the intensities of the mass are very similar to healthy breast tissues. After the MIFS scheme with different scaling coefficients, the enhanced results are shown in Fig. 11(b)–(d). It can be seen that the clarity of mass gradually degrades in these enhanced images. Compared with the original mammogram, there exist different degrees of integrity in Fig. 11(b)–(d) regarding the mammary marginal. The contrast ($C$) values of Fig. 10(a)–(d) are 0.3051, 0.4039, 0.3585, and 0.3095, and the RC values are 1.9229, 6.1252, 4.3111, and 2.1179. In our experiments, the sum of scaling coefficients is always set to 1. Fig. 11 suggests that low $a$ possibly produces not only high contrast of images but also high RC of ROIs, as well as the ambiguous mammary marginal,

TABLE II
PATIENT DEMOGRAPHICS AND CHARACTERISTICS

| Group | Patients[a] | Age (y)[b] | Images[c] | Pathology |
|---|---|---|---|---|
| #1 | 2 | 46.5 | 4 | Intraductal carcinoma |
| #2 | 3 | 61.3 | 6 | Invasive breast carcinoma |
| #3 | 3 | 49.7 | 6 | Invasive ductal carcinoma |
| #4 | 2 | 40.5 | 4 | Adenofibroma |
| #5 | 2 | 57.0 | 4 | Simple carcinoma |
| #6 | 2 | 65.0 | 4 | Intraductal papilloma |
| #7 | 2 | 63.5 | 4 | Papillary cystic neoplasm |

[a]Number of patients.
[b]Data are averages.
[c]Number of mammograms.

TABLE III
SUBJECTIVE COMPARISON OF ORIGINAL AND PROCESSED MAMMOGRAMS OBTAINED BY USING DIFFERENT ALGORITHMS

| Expert | #1 | #2 | #3 | #4 | #5 | Average |
|---|---|---|---|---|---|---|
| Original | 2.5132 | 2.2646 | 3.2944 | 3.0949 | 3.1080 | 2.8550 |
| ZIM | 2.5208 | 2.7804 | 3.5408 | 3.6041 | 3.0542 | 3.1000 |
| LEM | 3.3768 | 2.5305 | 3.3557 | 2.8891 | 3.2056 | 3.0715 |
| RUM | 2.9978 | 1.6586 | 2.3994 | 1.9675 | 2.5819 | 2.3210 |
| NUM | 2.5232 | 2.2518 | 2.9341 | 2.7147 | 2.7509 | 2.6350 |
| NILC | 2.7402 | 2.5171 | 3.2683 | 3.1183 | 2.9766 | 2.9241 |
| FBF | 2.9431 | 2.2581 | 2.9943 | 2.6702 | 2.8895 | 2.7510 |
| MIFS | 4.0753 | 3.7185 | 3.8046 | 3.9095 | 3.7118 | 3.8439 |

TABLE IV
COMPARISON OF CONTRAST VALUES FOR EACH GROUP OF ORIGINAL AND ENHANCED MAMMOGRAMS OBTAINED BY USING DIFFERENT ALGORITHMS

| Group | #1 | #2 | #3 | #4 | #5 | #6 | #7 |
|---|---|---|---|---|---|---|---|
| Ori. | 0.3003 | 0.3603 | 0.4916 | 0.4246 | 0.3998 | 0.4632 | 0.6152 |
| ZIM | 0.2761 | 0.3298 | 0.4424 | 0.3775 | 0.3669 | 0.4103 | 0.5575 |
| LEM | 0.3244 | 0.3867 | 0.5306 | 0.4669 | 0.4309 | 0.5067 | 0.6573 |
| RUM | 0.2466 | 0.2952 | 0.2957 | 0.2970 | 0.2443 | 0.3089 | 0.3597 |
| NUM | 0.3006 | 0.3605 | 0.4920 | 0.4246 | 0.3999 | 0.4638 | 0.6155 |
| NILC | 0.2499 | 0.2817 | 0.3942 | 0.3097 | 0.3408 | 0.3569 | 0.4089 |
| FBF | 0.3043 | 0.3657 | 0.4918 | 0.4246 | 0.3999 | 0.4632 | 0.6152 |
| MIFS | 0.4207 | 0.5011 | 0.6296 | 0.6335 | 0.5136 | 0.6144 | 0.7571 |

Note: Ori. denotes original mammograms. A higher value suggests the better enhancement performance.

TABLE V
COMPARISON OF CONTRAST IMPROVEMENT VALUES FOR EACH GROUP OF ORIGINAL AND ENHANCED IMAGES OBTAINED BY USING DIFFERENT METHODS

| Group | #1 | #2 | #3 | #4 | #5 | #6 | #7 |
|---|---|---|---|---|---|---|---|
| ZIM | 0.9193 | 0.9152 | 0.8999 | 0.8891 | 0.9176 | 0.8857 | 0.9063 |
| LEM | 1.0804 | 1.0734 | 1.0794 | 1.0996 | 1.0777 | 1.0939 | 1.0684 |
| RUM | 0.8211 | 0.8193 | 0.6014 | 0.6994 | 0.6111 | 0.6669 | 0.5847 |
| NUM | 1.0010 | 1.0005 | 1.0007 | 1.0000 | 1.0002 | 1.0014 | 1.0005 |
| NILC | 0.8321 | 0.7818 | 0.8017 | 0.7293 | 0.8524 | 0.7704 | 0.6647 |
| FBF | 1.0134 | 1.0149 | 1.0004 | 1.000 | 1.0002 | 1.0001 | 1.0001 |
| MIFS | 1.4008 | 1.3908 | 1.2806 | 1.4921 | 1.2846 | 1.3264 | 1.2307 |

TABLE VI
COMPARISON OF REGION CONTRAST VALUES FOR EACH GROUP OF ORIGINAL AND ENHANCED MAMMOGRAMS OBTAINED BY USING DIVERSE METHODS

| Group | #1 | #2 | #3 | #4 | #5 | #6 | #7 |
|---|---|---|---|---|---|---|---|
| Ori. | 1.5064 | 1.2163 | 2.4499 | 1.9050 | 1.8571 | 1.5491 | 1.5873 |
| ZIM | 2.1702 | 1.6328 | 3.0857 | 1.8455 | 1.9977 | 1.4161 | 1.6354 |
| LEM | 1.6722 | 1.2442 | 3.9166 | 1.9986 | 2.1677 | 2.0073 | 1.8766 |
| RUM | 1.7122 | 1.2505 | 3.4845 | 2.1498 | 1.9562 | 1.6176 | 1.0934 |
| NUM | 1.6590 | 1.2664 | 3.0408 | 1.9049 | 1.9632 | 1.6390 | 1.7018 |
| NILC | 2.5148 | 1.6935 | 4.6063 | 2.6522 | 2.3646 | 1.8988 | 1.8555 |
| FBF | 1.4829 | 1.0281 | 2.3906 | 1.3300 | 1.2977 | 1.1734 | 1.0121 |
| MIFS | 2.5803 | 1.9624 | 5.8578 | 3.7921 | 3.3986 | 3.6373 | 3.1642 |

TABLE VII
COMPARISON OF REGION CONTRAST IMPROVEMENT VALUES FOR EACH GROUP OF ORIGINAL AND ENHANCED IMAGES OBTAINED BY USING DIVERSE METHODS

| Group | #1 | #2 | #3 | #4 | #5 | #6 | #7 |
|---|---|---|---|---|---|---|---|
| ZIM | 1.4407 | 1.3425 | 1.2595 | 0.9688 | 1.0757 | 0.9141 | 1.0303 |
| LEM | 1.1101 | 1.0230 | 1.5987 | 1.0491 | 1.1673 | 1.2958 | 1.1823 |
| RUM | 1.1366 | 1.0282 | 1.4223 | 1.1285 | 1.0534 | 1.0442 | 0.6889 |
| NUM | 1.1013 | 1.0412 | 1.2412 | 0.9999 | 1.0572 | 1.0580 | 1.0721 |
| NILC | 1.6694 | 1.3923 | 1.8802 | 1.3922 | 1.2733 | 1.2257 | 1.1690 |
| FBF | 0.9844 | 0.8453 | 0.9758 | 0.6982 | 0.6988 | 0.7574 | 0.6376 |
| MIFS | 1.7130 | 1.6134 | 2.3911 | 1.9906 | 1.8301 | 2.3480 | 1.9935 |

and vice versa. High contrast is helpful in finding subtle masses and/or microcalcifications, while distinct mammary marginal can avoid introducing confusion in images. Hence, the choice of scaling parameters is a trade-off between the contrast of ROIs and the integrity of mammary marginal. Maybe, the original mammogram superimposed by highlighted ROIs is useful in this case.

Moreover, by using a threshold on an image basis, an object with the same intensities might be a foreground object in one mammogram but a background object in another image. In this case, the detection accuracy and validity of abnormalities will be impacted by the threshold. This suggests that the selection /determining of threshold is important in the design of MIFS scheme. Accordingly, the potential effect of thresholds with respect to detection accuracy and validity on the MIFS design should be carefully considered. In many medical images, Otsu technique does not perform well in segmentation of foreground /background areas. However, we adopted 32 clinically acquired images to test the iterative strategy, and the experimental results demonstrate that the iterative strategy (Section III-B) can produce satisfactory results. Nevertheless, further research on the automatic or semi-automatic selection of appropriate threshold is very necessary, especially for subtle changes in mammograms.

However, there are several limitations to our study: First, the number of patients in our study is small, although the number of mammograms is relatively large compared with prior studies. (For MOS test, the number of mammograms in [2] is $19 \times 5 = 95$, while that is $32 \times 8 = 256$ in this study.). Accordingly, the results presented are insufficient to demonstrate the advantage of the proposed scheme in complex/particular practical applications. However, this points out prospects in future study. Also, the effectiveness of MIFS method should be further explored (for example, threshold, membership function, and hyperbolization operator), although the proposed MIFS scheme can improve the contrast and visual quality of abnormalities in mammograms to some extent. Especially for more subtle changes in images, more attention should be paid to those issues. Late, the fast version of current algorithm should be investigated since the process time must be reasonably short in practical applications. Considering the comparability of the simulation codes, we make a comparison in Table VIII with respect to process time among the ZIM, LEM, RUM, NUM, NILC, FBF, and MIFS methods. The conditions for our comparison experiments are as follows: PC with Intel Xeon 2.40 GHz CPU, 16G RAM, Windows 7, and MATLAB 2013a. As seen from Table VIII, the MIFS has relatively high process time. Consequently, the fast MIFS algorithm is urgent in the future research.

TABLE VIII
COMPARISON OF TIME EXPENDITURE (SECOND)

| Image | Fig. 6(a) | Fig. 6(b) | Fig. 6(c) | Fig. 6(d) |
|---|---|---|---|---|
| Size | 3920 × 1861 | 3944 × 1987 | 3836 × 1483 | 3872 × 1615 |
| ZIM | 20.93 | 22.96 | 16.49 | 18.07 |
| LEM | 1.94 | 2.35 | 1.80 | 1.58 |
| RUM | 2.43 | 2.76 | 2.05 | 2.10 |
| NUM | 3.68 | 4.36 | 3.01 | 3.05 |
| NILC | 1.03 | 1.18 | 0.74 | 0.84 |
| FBF | 98.04 | 129.80 | 113.37 | 76.77 |
| MIFS | 19.09 | 20.96 | 14.52 | 16.28 |

## V. CONCLUSION

This paper proposes a novel IFS-based scheme called MIFS for mammogram enhancement. The proposed scheme initially separates a mammogram into the foreground/background areas, subsequently followed by different intuitionistic fuzzification, hyperbolization, and defuzzification operations implemented on each area and then achieves an enhanced result through nonlinear fusion operators. The MIFS scheme provides more robustness and flexibility, in order to accommodate more specific/complex needs in applications. In comparison to baseline methods, such as the ZIM, LEM, RUM, NUM, NILC, and FBF, the MIFS has better performance for improving both the contrast and visual quality of abnormalities in mammograms (such as the masses and/or microcalcifications) and makes these particular ROIs more recognizable. Experimental results indicate that the MIFS has much potential for detecting and diagnosing breast diseases in early stages. In the future, we will keep improving the current method from diverse directions, for example, the fast version, the threshold in the division of foreground/background area, and the flexibility in cases with heavy interference.

## REFERENCES

[1] R. Siegel *et al.*, "Cancer statistics, 2014," *CA Cancer J. Clin.*, vol. 64, no. 1, pp. 9–29, Jan. 2014.
[2] K. Panetta *et al.*, "Nonlinear unsharp masking for mammogram enhancement," *IEEE Trans. Inf. Technol. Biomed.*, vol. 15, no. 6, pp. 918–928, Nov. 2011.

[3] W. M. Morrow and R. B. Paranjape, "Region-based contrast enhancement of mammograms," *IEEE Trans. Med. Imag.*, vol. 11, no. 3, pp. 392–406, Sep. 1992.
[4] X. Gao *et al.*, "On combining morphological component analysis and concentric morphology model for mammographic mass detection," *IEEE Trans. Inf. Technol. Biomed.*, vol. 14, no. 2, pp. 266–273, Mar. 2010.
[5] L. E. Pace and N. L. Keating, "A systematic assessment of benefits and risks to guide breast cancer screening decision," *JAMA*, vol. 311, no. 13, pp. 1372–1335, Apr. 2014.
[6] B. A. Nikola and J. Peter, "Abolishing mammography screening programs? A view from the Swiss medical board," *N. Engl. J. Med.*, vol. 370, no. 21, pp. 1965–1967, May 2014.
[7] R. A. Smith *et al.*, "American cancer society guidelines for the early detection of cancer," *CA Cancer J. Clin.*, vol. 56, no. 1, pp. 11–25, Jan. 2006.
[8] A. K. Mohideen and K. Thangavel, "Region-based contrast enhancement of digital mammograms using an improved watershed segmentation," *Int. J. Image Grap.*, vol. 13, no. 1, pp. 1350007-1–1350007-25, Jan. 2013.
[9] N. Petrick *et al.*, "An adaptive density-weighted contrast enhancement filter for mammographic breast mass detection," *IEEE Trans. Med. Imag.*, vol. 15, no. 1, pp. 59–67, Feb. 1996.
[10] J. Tang *et al.*, "A direct image contrast enhancement algorithm in the wavelet domain for screening mammograms," *IEEE J. Sel. Topics Signal Process.*, vol. 3, no. 1, pp. 74–80, Feb. 2009.
[11] J. Bozek *et al.*, "A survey of image processing algorithms in digital mammography," *Rec. Advan. Mult. Sig. Process. Commun.*, vol. 231, pp. 631–657, 2009.
[12] H. D. Cheng *et al.*, "Computer-aided detection and classification of microcalcifications in mammograms: A survey," *Pattern Recognit*., vol. 36, no. 12, pp. 2967–2991, Dec. 2003.
[13] J. Tang *et al.*, "Computer-aided detection and diagnosis of breast cancer with mammography: Recent advances," *IEEE Trans. Inf. Technol. Biomed.*, vol. 13, no. 2, pp. 236–251, Mar. 2009.
[14] A. Papadopoulos *et al.*, "Improvement of microcalcification cluster detection in mammography utilizing image enhancement techniques," *Comput. Biol. Med.*, vol. 38, no. 10, pp. 1045–1055, 2008.
[15] H. D. Lin *et al.*, "Statistical based subband filtering technique for digital mammogram enhancement," *Biomed Engrg. Appl. Basis Commun.*, vol. 15, no. 4, pp. 150–156, Aug. 2003.
[16] A. P. Dhawan *et al.*, "Enhancement of mammographic features by optimal adaptive neighborhood image processing," *IEEE Trans. Med. Imag.*, vol. 5, no. 1, pp. 8–15, Jan. 1986.
[17] J. K. Kim *et al.*, "Adaptive mammographic image enhancement using first derivative and local statistics," *IEEE Trans. Med. Imag.*, vol. 16, no. 5, pp. 495–502, Oct. 1997.
[18] S. D. Chen and A. R. Ramli, "Minimum mean brightness error bi- histogram equalization in contrast enhancement," *IEEE Trans. Consum. Electr.*, vol. 49, no. 4, pp. 1310–1319, Nov. 2003.
[19] G. Ramponi and A. Polesel, "Rational unsharp masking technique," *J. Electron. Imag.*, vol. 7, no. 2, pp. 333–338, Apr. 1998.
[20] R. Sivaramakrishna *et al.*, "Comparing the performance of mammographic enhancement algorithms," *Amer. J. Roentgol.*, vol. 175, no. 1, pp. 45–51, Jul. 2000.
[21] A. Laine *et al.*, "Wavelets for contrast enhancement of digital mammography," *IEEE Eng. Med. Biol. Mag.*, vol. 14, no. 5, pp. 536–550, Sep./Oct. 1995.
[22] A. Mencattini *et al.*, "Mammographic images enhancement and denoising for breast cancer detection using dyadic wavelet processing," *IEEE Trans. Instrum. Meas.*, vol. 57, no. 7, pp. 1422–1430, Jul. 2008.
[23] P. Heinlein *et al.*, "Integrated wavelets for enhancement of microcalcifications in digital mammography," *IEEE Trans. Med. Imag.*, vol. 22, no. 3, pp. 402–413, Mar. 2003.
[24] P. Y. Liu and H. X. Li, "Fuzzy techniques in image restoration research—A survey," *Int. J. Comput. Cognit.*, vol. 2, no. 2, pp. 131–149, Feb. 2004.
[25] S. Das and M. K. Kundu, "A neuro-fuzzy approach for medical image fusion," *IEEE Trans. Bio. Eng.*, vol. 60, no. 12, pp. 3347–3353, Dec. 2013.
[26] M. E. Yuksel and A. Basturk, "Application of type-2 fuzzy logic filtering to reduce noise in color images," *IEEE Comput. Intell. Mag.*, vol. 7, no. 3, pp. 25–35, Aug. 2012.
[27] F. Russo, "Recent advances in fuzzy techniques for image enhancement," *IEEE Trans. Instrum. Meas.*, vol. 47, no. 6, pp. 1428–1434, Dec. 1998.
[28] C. Yang *et al.*, "A fuzzy-statistics-based principal component analysis (FS-PCA) method for multispectral image enhancement and display," *IEEE Trans. Geosci. Remote Sens.*, vol. 46, no. 11, pp. 3937–3947, Nov. 2008.
[29] O. Gloger *et al.*, "Fully automated renal tissue volumetry in MR volume data using prior-shape-based segmentation in subject-specific probability maps," *IEEE Trans. Bio. Eng.*, vol. 62, no. 10, pp. 2338–2351, Oct. 2015.
[30] D. R. Wu, "Approaches for reducing the computational cost of interval type-2 fuzzy logic systems: Overview and comparisons," *IEEE Trans. Fuzzy Syst.*, vol. 21, no. 1, pp. 80–99, May 2013.
[31] H. D. Cheng *et al.*, "A novel approach to microcalcification detection using fuzzy logic technique," *IEEE Trans. Med. Imag.*, vol. 17, no. 3, pp. 442–450, Jun. 1998.
[32] H. D. Cheng and H. Xu, "A novel fuzzy logic approach to mammogram contrast enhancement," *Inf. Sci.*, vol. 148, pp. 167–184, Dec. 2002.
[33] M. E. Algorri and F. Flores-Mangas, "Classification of anatomical structures in mr brain images using fuzzy parameters," *IEEE Trans. Bio. Eng.*, vol. 51, no. 9, pp. 1599–1608, Sep. 2004.
[34] S. Aghagolzadeh and O. K. Ersoy, "Transform image enhancement," *Opt. Eng.*, vol. 31, no. 3, pp. 614–626, Mar. 1992.
[35] S. K. Pal and R. A. King, "Image enhancement using smoothing with fuzzy sets," *IEEE Trans. Syst., Man, Cybern.*, vol. 11, no. 7, pp.494–501, Jul. 1981.
[36] H. R. Tizhoosh, *Fuzzy Technique in Image Processing*. Berlin, Germany: Springer-Verlag, 2000, pp.137–146.
[37] J. M. Mendel and R. I. B. John, "Type-2 fuzzy sets made simple," *IEEE Trans. Fuzzy Syst.*, vol. 10, no. 2, pp. 117–127, Apr. 2002.
[38] T. Chaira, "Intuitionistic fuzzy segmentation of medical images," *IEEE Trans. Bio. Eng.*, vol. 57, no. 6, pp. 1430–1436, Jun. 2010.
[39] I. Montes *et al.*, "Divergence measures for intuitionistic fuzzy sets," *IEEE Trans. Fuzzy Syst.*, vol. 23, no. 2, pp. 444–456, Apr. 2014.
[40] K. P. Lin, "A novel evolutionary kernel intuitionistic fuzzy *c*-means clustering algorithm," *IEEE Trans. Fuzzy Syst.*, vol. 22, no. 5, pp. 1074–1087, Aug. 2013.
[41] M. M. Mushrif and A. K. Ray, "A-IFS histon based multithresholding algorithm for color image segmentation," *IEEE Signal Process*., vol. 16, no. 3, pp. 168–171, Mar. 2009.
[42] V. P. Ananthi *et al.*, "Segmentation of gray scale image based on intuitionistic fuzzy sets constructed from several membership functions," *Pattern Recognit*., vol. 47, no. 12, pp. 3870–3880, Dec. 2014.
[43] E. Szmidt and J. Kacprzyk, "Entropy for intuitionistic fuzzy set," *Fuzzy Sets Syst.*, vol. 118, no. 3, pp. 467–477, Mar. 2001.
[44] K. T. Atanassov, "Intuitionistic fuzzy set," *Fuzzy Set. Syst.*, vol. 20, no. 1, pp. 87–96, Aug. 1986.
[45] H. Bustunce *et al.*, "Restricted equivalence functions," *Fuzzy Sets Syst.*, vol. 157, no. 17, pp. 2333–2346, Sep. 2006.
[46] H. D. Cheng *et al.*, "Approaches for automated detected and classification of masses in mammograms," *Pattern Recognit*., vol. 36, no. 4, pp. 646–668, Apr. 2006.
[47] S. T. Wang *et al.*, "A novel image thresholding method based on Parzen window estimate," *Pattern Recognit*., vol. 41, no. 1, pp. 117–129, Jan. 2008.
[48] K. Panetta *et al.*, "Parameterized logarithmic framework for image enhancement, " *IEEE Trans. Syst., Man, Cybern. B, Cybern.*, vol. 41, no. 2, pp. 460–473, Apr. 2011.
[49] T. L. Kong and N. A. M. Isa, "Histogram based image enhancement for non-uniformly illuminated and low contrast images," in *Proc. IEEE ICIEA*, 2015, pp. 586–591.
[50] K. N. Chaudhury, "Acceleration of the shiftable $O(1)$ algorithm for bilateral filtering and nonlocal means," *IEEE Trans. Image Process.*, vol. 22, no. 4, pp. 1291–1300, Apr. 2013.

Authors' photographs and biographies not available at the time of publication.